Metallurgical and Materials Transactions A 45 (2014) 4916-4931

White-etching matter in bearing steel Part 2: Distinguishing cause and effect in bearing steel failure

W. Solano-Alvarez[a], H. K. D. H. Bhadeshia[a]

[a]*Materials Science and Metallurgy, University of Cambridge, U.K*

Abstract

The premature failure of large bearings of the type used in wind turbines, possibly through a mechanism called "white-structure flaking", has triggered many studies of microstructural damage associated with "white-etching areas" created during rolling contact fatigue, although whether they are symptoms or causes of failure is less clear. Therefore, some special experiments have been conducted to prove that white-etching areas are the consequence, and not the cause, of damage. By artificially introducing a fine dispersion of microcracks in the steel through heat treatment and then subjecting the sample to rolling contact fatigue, manifestations of hard white-etching matter have been created to a much greater extent than samples similarly tested without initial cracks. A wide variety of characterisation tools has been used to corroborate that the white areas thus created have the same properties as reported observations on real bearings. Evidence suggests that the formation mechanism of the white-etching regions involves the rubbing and beating of the free surfaces of cracks, debonded inclusions, and voids under repeated rolling contact. It follows that the focus in avoiding early failure should be in enhancing the toughness of the bearing steel in order to avoid the initial microscopic feature event.

Keywords: bearing steel, white-etching areas, cracked martensite, rolling contact fatigue, butterflies

1. Introduction

White structure flaking is a bearing failure mechanism associated with microstructural damage known commonly as "white-etching matter" (WEM), that leads eventually to flakes of material detaching from the raceway surface. Such damage has been identified as one of the possible causes of the premature failure of large bearings, such as those in wind-turbine gearboxes [1]. White-etching matter is a generic term describing microstructural damage that exhibits lighter contrast relative to the surrounding material, when an etched sample is observed using optical microscopy. This diminished contrast arises because the wavelength of light (390-770 nm) is large compared with the size of crystallites in the affected regions (5-500 nm) [2]. White-etching regions include the so-called butterfly wings, some cracks, white-etching spheres, bands, all caused by rolling contact fatigue (RCF) in the subsurface of bearing raceways or white-etching layers caused again by rolling contact fatigue of railway tracks or by hard turning, as reviewed in [3]. In the case of bearings, rolling contact fatigue refers to the cyclic loading of the raceways by the repeated passage of rolling elements, that induce Hertzian contact stresses responsible for phenomena such as the decomposition of retained austenite, smoothing of surfaces, steady-state plastic strain, texture development, residual stress development, work hardening, and surface or subsurface crack initiation and propagation.

WEM can be classified into two categories, hard and soft [3]. Soft white-etching matter such as that associated with bands, is depleted in carbon [4], can be transgranular [5], and is composed of fine, equiaxed grains that have recrystallised [6]. Such regions can also contain amorphous patches and microvoids, whilst the material adjacent to the band has a high dislocation density [7]. It is emphasised that these soft white-etching bands are not associated with cracks or surface discontinuities, unlike the harder versions. The latter occur as butterflies, cracks, or spheres, and are some 30-50% harder than the unaffected matrix [8, 9]. They are generally supersaturated in carbon as a result of carbide dissolution [10], have a structure of equiaxed but very fine grains [7, 11, 12], and are free of large carbides [11, 12]. In the case of butterflies, the hard white-etching matter wings originate at voids, non-metallic inclusions, carbides, or microcracks already at 5-10% of the L_{10} life, which represents the number of loading cycles when 10% of the bearings in a population fail before their estimated life time[1, 13].

Several mechanisms have been proposed to explain the formation of WEM. The hard layers are associated with severe, localised plastic deformation with the possibility of some dynamic recovery [14–16]. The white-etching layers on railway tracks where rolling contact and sliding dominate the damage process, some authors consider carbide dissolution under the influence of deformation to be the primary mechanism [17] whereas others conclude that the structural change is due to rapid reaustenitisation followed by martensitic transformation [18]. An alternative interpretation relies on the formation of adiabatic shear leading to localised severe plasticity [19], although there are difficulties in reconciling the onset of adiabatic shear with the observed band dimensions and necessary strain rates [3]. There have also been reports that the process of WEM formation involves a combination of corrosion fatigue, hydrogen ingress and the tribochemical dissolution of inclusions [20]. The fundamental question that needs to be addressed is whether the white-etching regions are a cause or symptom of the onset of damage; this is the issue addressed in the present work.

2. Experimental Methods

2.1. Material

The material used for this study is an Ovako hot-rolled and spheroidised 52100 steel rod with the composition described in Table 1.

Table 1: Chemical composition, wt%, of the 52100 steel used.

C	Cr	Mn	Mo	Si	Ni	Al	P	S	Cu	Co	Ca	Ti
0.98	1.38	0.28	0.06	0.28	0.18	0.04	0.010	0.017	0.21	0.015	0.001	<0.001

2.2. Microscopic cracking

Long cylindrical samples 10 mm in diameter and 120 mm long were manufactured from the sample material using a spark erosion machine and a lathe, followed by heat-treatment in a standard Carbolite RWF1200 box furnace. Three different heat treatments were applied to obtain the standard and two different cracked microstructures. The crack-free control sample

was austenitised at 1113 K (840 °C) for 10 min, quenched in *GP460* oil at room temperature, and tempered at 433 K (160 °C) for 2 h, representing the standard heat treatment for 52100 steel. The sample containing cracked martensite-plates (MPC) was austenitised at 1313 K (1040 °C) for 90 min, cooled in air for 50 s, quenched in *GP460* oil at room temperature, and finally tempered at 433 K (160 °C) for 2 h. After the heat treatment, these two samples were cylindrically ground to the final diameter of 9.53 mm to get rid of any decarburised layer and to achieve a reasonable surface roughness for rolling-contact fatigue testing.

The surface cracked sample (SC) was asutenitised at 1313 K (1040 °C) for 30 min, cooled in air for 50 s, followed by quenching in *GP460* oil at room temperature. This was then indented twelve times along its circumference using a Vickers indenter and a 130 kg load to induce indentation cracks before cylindrically grinding to the final diameter of 9.53 mm. The grinding eliminated the upheavals caused by indentation but not the surface-breaking indent cracks; after grinding, it was finally tempered at 433 K (160 °C) for 2 h. Temperatures were monitored throughout the heat treatment of all samples by spot welding K-type thermocouples to the samples. The specific details of the crack-inducing heat-treatments are described in more detail in [21].

2.3. Rolling contact fatigue

Testing was carried out on a Delta Research Corporation BR-4 Ball-Rod Rolling Contact Fatigue machine [22]. The load is applied by three 12.7 mm in diameter balls, placed inside a bronze retainer, so that the balls push against the rotating test specimen of 9.53 mm in diameter through two tapered bearing cups held at a certain distance of each other by adjusting the length of three springs, as seen on Fig. 1. Testing was performed at room temperature without transient conditions or hydrogen charging of the specimens that would accelerate, but might also alter the microstructural degradation process.

Before every test, three new 52100 balls with a surface roughness of 0.013 µm, the bronze retainer, and the rod specimen were ultrasonically cleaned for 5 min first in a mixture of 50% isopropanol-50% water, then in acetone, and finally in isopropanol. The tapered loading cups were changed every four tests and turbine oil *BP2380* was used as a lubricant at room

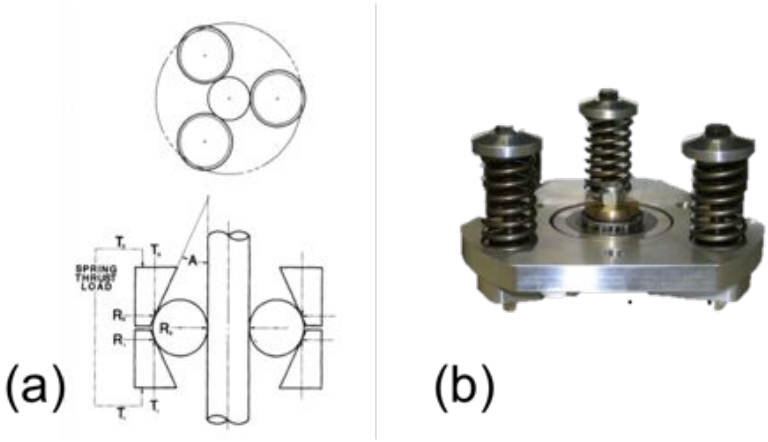

Figure 1: a) Rotating cylinder specimen stressed by three radially-loaded balls, which are thrust loaded by three compression springs [23], and b) individual retainer plate during the load setting configuration showing the three compression springs around three calibration bolts.

temperature and a rate of 10 drops min^{-1}. This oil was filtered and recirculated. Vibration levels were monitored through an accelerometer, which automatically stopped tests if the thresholds were surpassed, caused normally only by flaking or spalling. All tests were performed at a rotational speed of 3600 rpm (the design of the test rig allows ∼2.4 stress cycles per revolution) and a Hertzian pressure of 3.5 GPa (191 N of load). The values and depths of the maximum unidirectional and orthogonal shear stresses induced by such Hertzian pressure are presented in Table 2.

Table 2: Maximum shear stress, τ_{max}, acting at ±45° with respect to the surface, and orthogonal shear stress $\tau_{xz,max}$, acting parallel and normal to surface, subsurface shear stresses and their depths, for circular contact. The values assume frictionless and elastic Hertzian contact at 3.5 GPa [24].

Dimension	τ_{max}		$\tau_{xz,max}$	
	GPa	Depth / μm	GPa	Depth / μm
Circular contact	1.09	190	0.88	99

2.4. Characterisation

Before RCF testing, the average surface roughness, R_a, of the cylindrically ground specimens was measured using a Veeco Dektak 6M Stylus Profiler, which has a tip radius of 12.5 µm. Given the shape of the specimens, the roughness was measured along the length; the surface over which the balls rotate is likely to be significantly smoother given the nature of the final grinding process.

Optical and scanning electron microscopy (SEM) using a Zeiss optical microscope and a JEOL JSM 5500LV microscope were performed on test specimens prior to heat treatment, after heat treatment, and after RCF. For such characterisation, RCF specimens were cut along the centre of the racetrack in the circumferential cross section and also along the longitudinal section (Fig. 2).

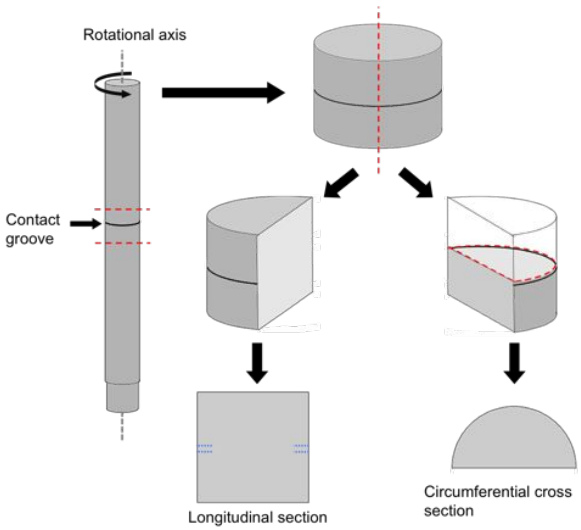

Figure 2: Cutting procedure and sections of RCF test specimens.

The process of microstructural degradation around cracks and inclusions was characterised in more detail by carving out lamellae of white-etching cracks and butterflies from RCF samples, at different cycles, using a FEI Helios dual beam field emission SEM/FIB. These lamellae were then observed using a JEOL 200CX transmission electron microscope (TEM) to obtain images and diffraction patters of the matrix, white-etching matter, and inclusions. The chemical compositions of the WEM of butterflies and cracks

(WECs), butterfly inclusions, and fatigue crack initiating inclusions were studied using EDS with an Oxford Instruments detector in the JEOL JSM 5500LV SEM and a EDAX r-TEM ultra-thin window (UTW) X-ray detector in the FEI Tecnai F20-G2 FEG-STEM in case of the FIB lamellae.

Although the main objective of this work was to establish whether WEM results from the collision of crack faces during RCF, butterflies were also studied as their WEM wings have been well characterised and would provide a bridge between the WEM created in this study and observations in the published literature.

2.4.1. Macro- and Nano-hardness

Since the crack-free (standard heat treatment) and pre-cracked samples were austenitised at different temperatures and times, their RCF responses were compared by taking into account differences in macrohardness and retained austenite. Macrohardness of the three differently heat-treated samples was evaluated using a Vickers indenter and a 30 kg load. Instead, an MTS Nanoindenter XP with a pyramidal Berkovich tip was used to perform nanoindentations on the white-etching matter around cracks and inclusions formed after RCF in order to determine its hardness compared with the matrix. Such measurements were performed at a constant depth of 1 µm. In each case, the mean and standard error reported correspond to ten indentations.

2.4.2. X-Ray Diffraction

The retained austenite content was determined using a Philips PW1830 vertical diffractometer with a CuK_α radiation. Scans were performed from 30 to 125 °, with a step size of 0.05 ° and a dwell time of 26 s. A divergence slit of 0.5 °, an anti-scatter slit of 0.5 °, and a receiving slit of 0.2 mm were used to restrict the beam size and the counts obtained. A rotating stage was necessary for sample MPC in order to obtain sufficient counts due the larger size of its grains. Once the patterns were obtained, High Score plus and the Rietveld refinement method were used to fit body-centred tetragonal martensite to two isolated martensite peaks (020 and 121) for each spectrum. This pair of values of tetragonality were then used as minimum and maximum limits in the fitting of lattice parameters for martensite using either the whole

spectrum or a cropped version, which eliminated martensite and austenite overlapping peaks (e.g. $110_{\alpha'}$ and 111_{γ}). Finally, the three control sample spectra were analysed accounting for cementite, using the whole spectra and the respective martensite tetragonality values.

2.4.3. Electron Backscattered Diffraction

EBSD was performed on colloidal silica polished samples using a Camscan MX2600 FEG-SEM in order to study the propensity of cracks nucleated at inclusions during RCF to propagate along prior austenite grain boundaries in order to evidence the lack of toughness of 52100 steel that is the alleged cause of WEM (through the processes of crack formation and rubbing). Toughness is here used to indicate the ability of the alloy to resist crack formation at impurities or defects during cyclic deformation, leading to propagation along prior austenite grain boundaries and ultimately, macroscopic failure.

It is important to note that the cracks studied through EBSD were almost certainly not caused by the cracking heat treatments, but by RCF as will be explained later. Post-acquisition analysis of the patterns included removal of wrongly indexed points (wild spikes) and extrapolation of solution to non-indexed points first using non-iterative eight neighbouring points, then iterations with seven, and finally six neighbouring points.

3. Results

The as-received microstructure of the steel, consisting of ferrite and spheroidised cementite particles, is illustrated in Fig. 3. Once machined, the cylindrical test specimens were heat treated according to the standard, surface crack, and martensite plate crack procedures, resulting in the microstructures illustrated in Fig. 4. The Vickers hardness values of all these samples are presented in Table 3.

X-ray diffraction (XRD) measurements of the three different heat treatments applied were performed to take into account the difference of retained austenite volumes when analysing the WEM generated during RCF. The volume fractions of retained austenite were obtained via Rietveld refinement on samples quenched (Q) from the three different austenitisation temperatures

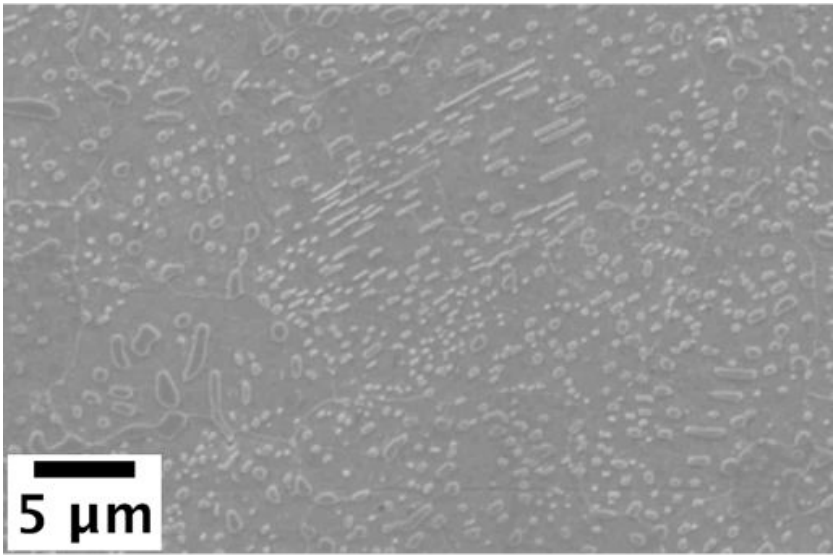

Figure 3: SEM image of initial spheroidised microstructure of the 52100 steel used.

Table 3: Hardness values of the as-received material, crack-free, surface cracked, and martensite plate cracked samples.

Sample	HV30
As-received	193±2
Control (standard heat-treatment)	794±5
Surface cracked (SC)	742±9
Martensite-plate cracked (MPC)	770±8

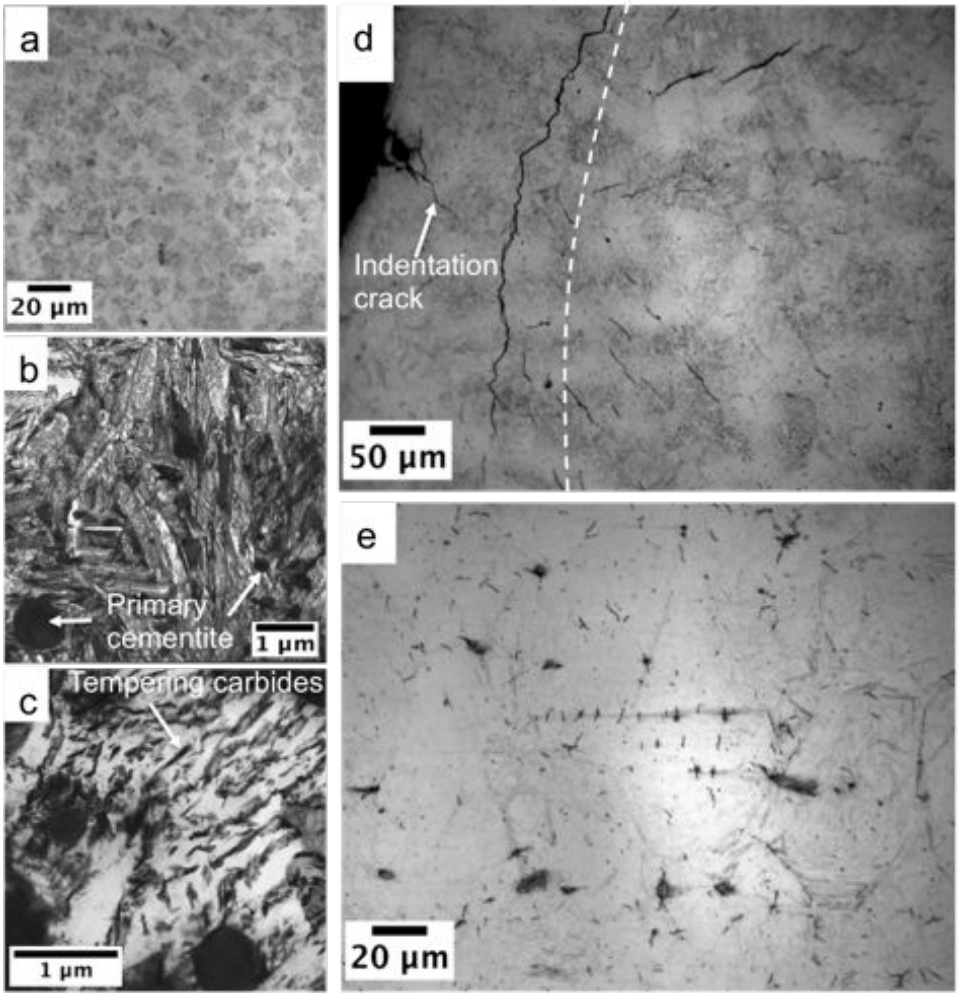

Figure 4: (a-c) Micrographs of crack-free sample produced using the industry standard heat treatment, resulting in a mixture of tempered martensite containing carbides, and primary cementite. (d) Surface cracked sample before cylindrical grinding. The dashed line represents the depth of material to be removed, which will leave behind a cracked, but indent-free surface. (e) Circumferential cross section of a cylindrical sample containing martensite plate cracks in the bulk (the region displayed is 4.7 mm deep).

and times, quenched and tempered (Q-T) using the standard tempering temperature 433 K (160 ℃) and time (2 h), and quenched, tempered, and RCF tested (Q-T-RCF). All values quoted have an uncertainty of ±0.01. The results are summarised in Table 4.

Table 4: Volume fraction austenite (V_γ) for control, SC, and MPC samples in the top part of the table, and austenite and cementite (V_θ) only for the control sample in the bottom half, which is the only sample with primary cementite particles.

Analysis method	Treatment	Volume fraction retained austenite		
		Control	Surface cracked SC	Martensite cracked MPC
tetragonality deduced from $020_{\alpha'}$ and $121_{\alpha'}$, only non-overlapping peaks used to determine γ content	Q	0.05	0.14	0.15
	Q-T	0.04	0.12	0.12
	Q-T-RCF	0.04	0.10	0.11
tetragonality deduced from $020_{\alpha'}$ and $121_{\alpha'}$, all peaks (including those that overlap) used to determine γ content	Q	0.06	0.16	0.14
	Q-T	0.05	0.12	0.12
	Q-T-RCF	0.05	0.08	0.11
		Control sample only		
		V_γ	V_θ	
tetragonality deduced from $020_{\alpha'}$ and $121_{\alpha'}$, all peaks (including those that overlap) used to determine volume %	Q	0.05	0.09	
	Q-T	0.04	0.05	
	Q-T-RCF	0.05	0.05	

After surface roughness measurements (table 5), the three different specimens were subjected to RCF testing until failure. The Hertzian pressure used (3.5 GPa) is greater than the normal wind turbine gearbox bearing operating pressure of 1-2 GPa [25], but was selected due to experimental time frames and test rig limitations. The results are presented in Table 6. Since the test specimens are 12 mm long, several RCF tests can be conducted on the same sample but at different positions along their lengths. These different tests are denoted by the number next to the sample identifier e.g. MPC-1 and MPC-2.

After RCF, the three samples were cut along the circumferential cross section and the longitudinal section as illustrated in Fig. 2. Careful metallographic preparation including nickel plating and mounting on hard bakelite (with silica or alumina additions) was needed to avoid rounding of the edges of the specimens where the majority of the RCF effects are manifested. Char-

Table 5: Average (R_a) and root mean squared (R_q) surface roughness values for each RCF specimen.

Sample	R_a / µm	R_q / µm
Control	0.08±0.02	0.13±0.04
SC	0.06±0.01	0.08±0.01
MPC	0.06±0.01	0.08±0.01

Table 6: RCF cycles for the crack-free (control) and pre-cracked samples (SC and MPC) all running at room temperature, 3600 rpm, and 3.5 GPa of Hertzian pressure.

Test	Cycles	Time / h	Reason of stoppage
Control-1	2.9×10^8	558.1	Excessive vibration
MPC-1	8.6×10^6	16.8	Lubrication system failure
MPC-2	2.8×10^8	551.2	Load bolt and spring got loose
SC-1	8.6×10^8	1672.5	Excessive vibration

acterisation of these regions was performed mainly using optical microscopy since white-etching matter is defined as such due to its relative colour when etched in nital. Under SEM, WEM does not necessarily appear brighter than the matrix, but can be differentiated due to topographical contrast. Fig. 5 shows an ensemble of optical and SEM micrographs of the most notorious WEM manifestations around cracks, although butterflies are also included, in each of the three samples tested under RCF.

The WEM generated around microcracks and inclusions during RCF was then characterised mechanically, optically, chemically, and crystallographically using nanoindentation, FIB/TEM, EDS, and EBSD in order to identify the type of WEM generated (hard or soft) and provide insights on its formation mechanisms. In the case of nanoindentation, only the sample containing martensite-plate cracks was analysed given the larger size of WEMs present that allowed indents to be fully contained in the WEM regions of either butterflies or cracks. These results are presented in Table 7. An image of some of the indented regions are shown in Fig. 6.

Following nanoindentation, WEM around cracks and inclusions was extracted from the bulk using focused ion beam machining according to the

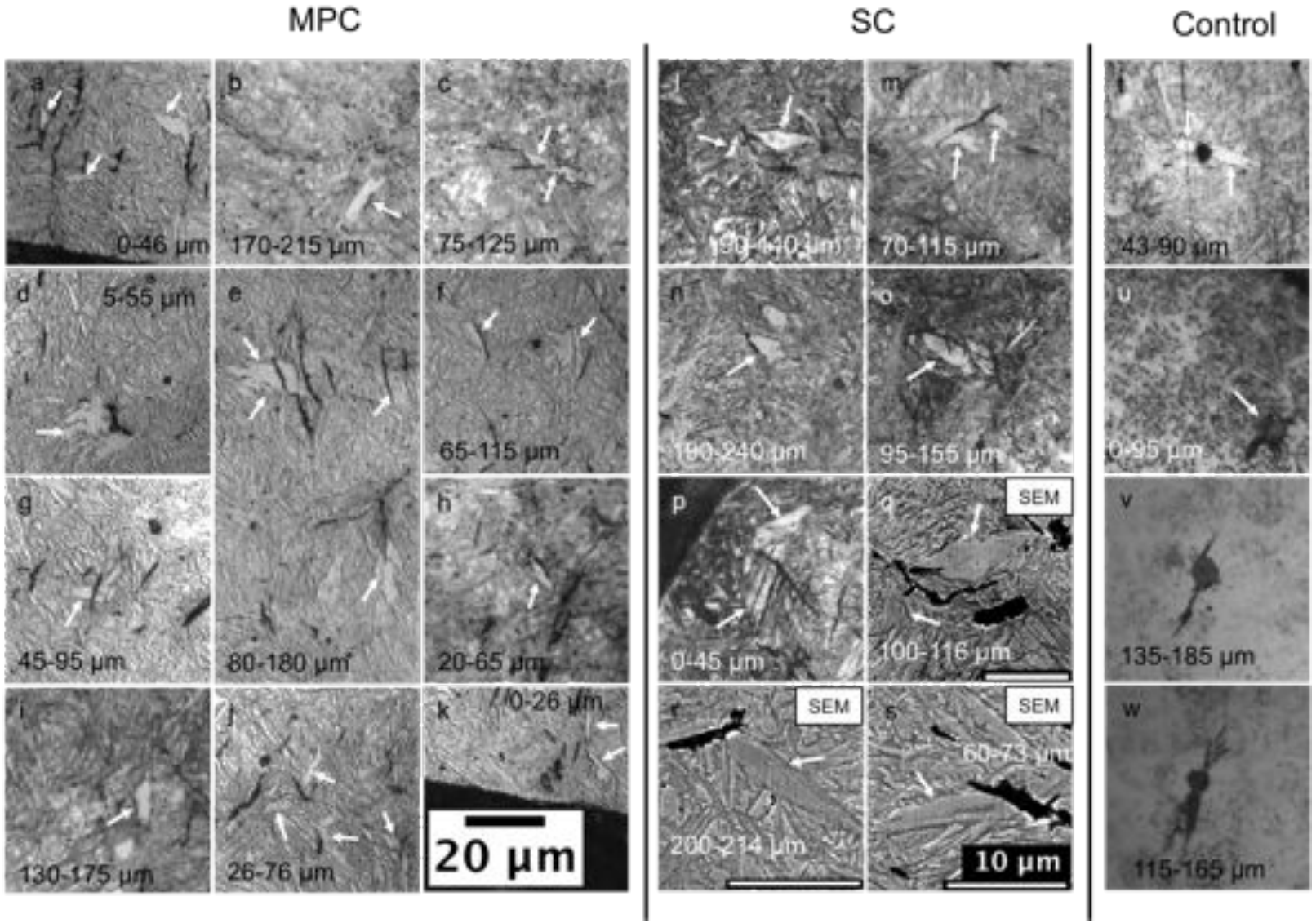

Figure 5: WEM regions around cracks and inclusions (butterflies): (a-k) MPC, (l-s) SC, and (t-w) Control. The depth range of the region photographed, relative to the contact surface is indicated on each image. The white arrows show the location of the WEM. All optical micrographs share the same magnification except for the 3 labelled SEM images.

Table 7: Nanohardness values of the WEM and matrix of sample MPC using a constant indentation depth of 1000 nm.

Region	Nanohardness / GPa
WEM	12.3±0.2
Matrix	11.3±0.6

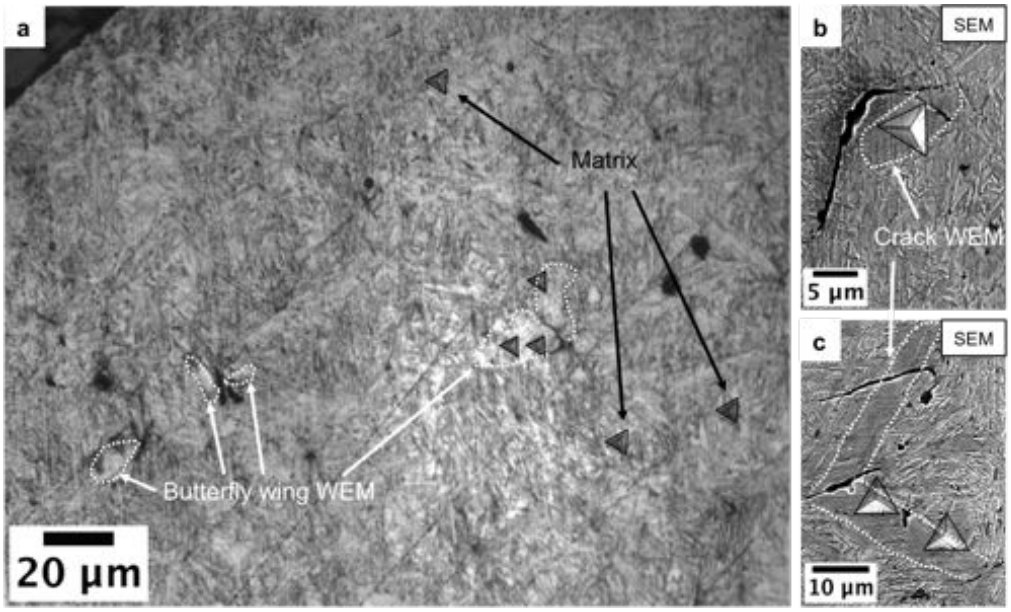

Figure 6: SEM image of some of the nanoindentations performed on the MPC sample.

sequence portrayed in Fig. 7. SEM images of the location of the extracted lamellae are shown in Fig. 8a and b along with TEM images of the lamellae themselves and diffraction patters of relevant features or regions. Finally, in Fig. 10, a sequence of SEM images of lamella-2 (crack in SC sample) at several stages during the FIB thinning process is presented to give a 3D insight of the result of cracked-surface rubbing after long testing times.

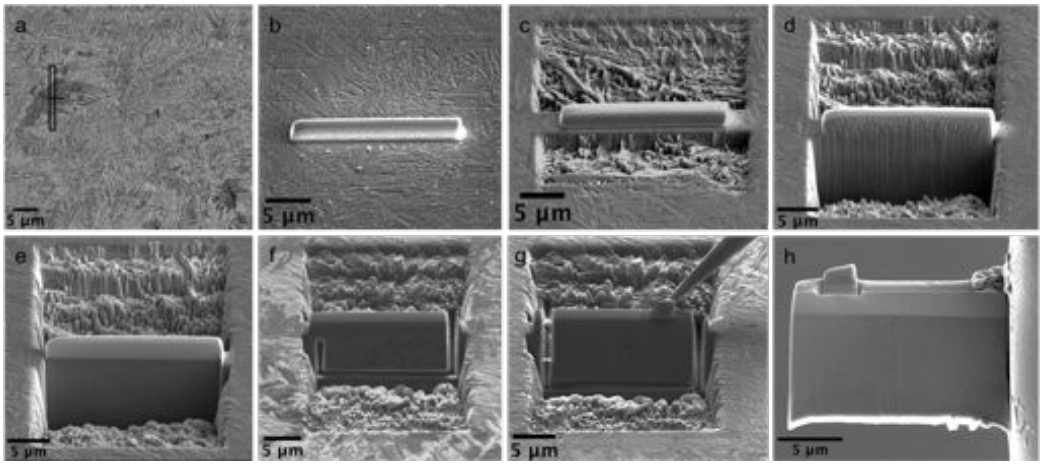

Figure 7: SEM of FIB sequence followed to study the material around cracks and inclusions by extraction of thin lamellae. This sequence refers particularly to lamella-3 (Fig. 9).

During microscopy of the circumferential cross section of the MPC specimen, a large crack approximately 1.7 mm long was found at a depth of around 400 µm. Its large dimensions and the considerable number of large inclusions entrapped in the path of the crack indicate that it might have formed during RCF. In order to determine its extent, the sample was sequentially ground and examined. Four cross sections are shown in Fig. 11. Throughout the sections, no connections of this crack with the free surface were found. The crack was analysed using electron backscatter diffraction (EBSD) (fig. 12) to determine if it propagated along the prior austenite grain boundaries, which would evidence the relatively poor toughness of 52100 steel. Furthermore, five inclusions found in section (d), but some still visible in (c), were analysed using EDS to determine their chemical composition.

Continuing with the characterisation of the WEM generated, energy dispersive spectroscopy (EDS) was used to determine the chemical composition of the WEM compared to the matrix as well as analyse the composition of

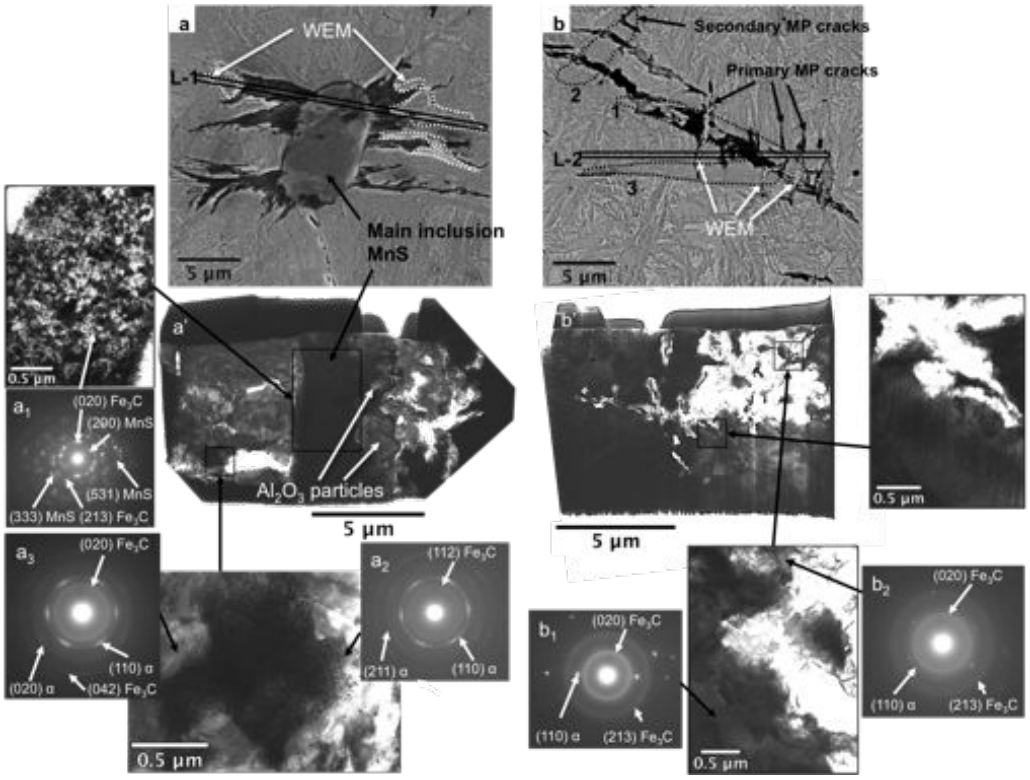

Figure 8: SEM image of FIB milling location and TEM image of extracted lamella for (a) inclusion 50 µm deep and (b) crack 120 µm deep both in SC sample tested for 1672.5 h (8.6×10^8 cycles).

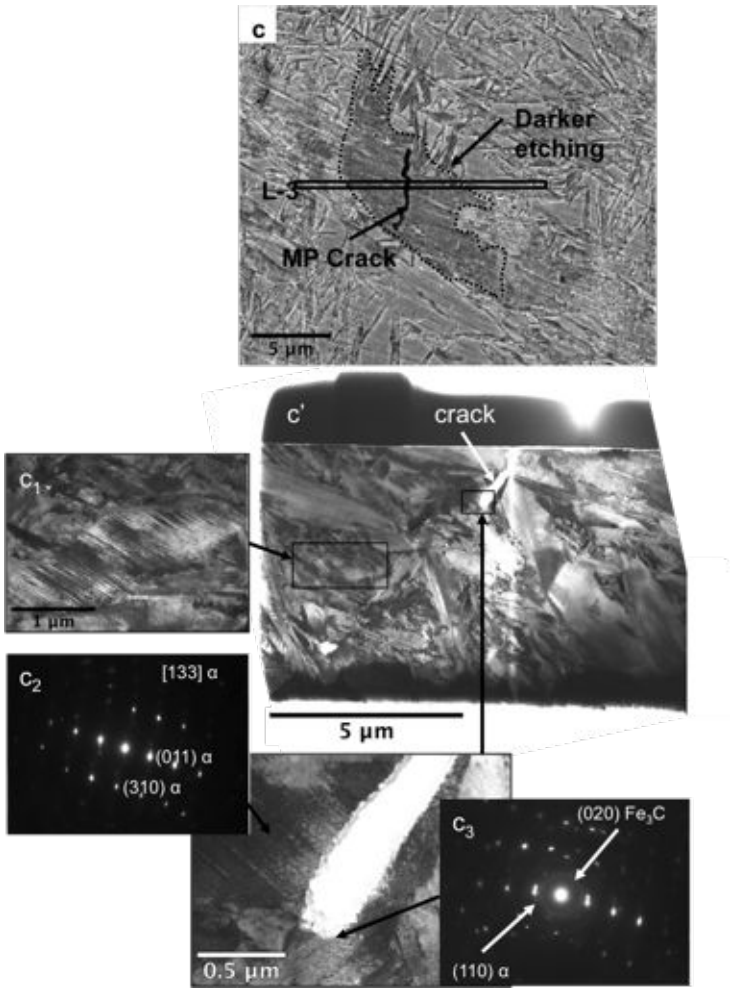

Figure 9: SEM image of FIB milling location and TEM image of extracted lamella for (c) crack 500 µm deep in MPC sample tested for 16.8 h (8.6×10^6 cycles).

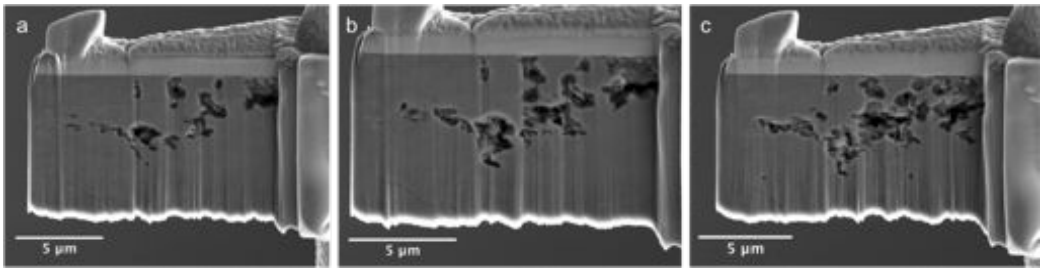

Figure 10: SEM images of serial cross sections of the crack in lamella-2 (crack in SC sample, 120 µm deep, tested at RCF for 1672 h) during FIB preparation.

inclusions that caused butterflies (lamella-1) and fatigue cracks (fig. 11). The results of this analysis are presented in Table 8.

4. Discussion

4.1. Heat treatments

As seen in fig. 4, the cracking heat treatments created a wide range of crack morphologies that allowed a detailed study of damage/ subsurface stress interaction. Whereas the MPC treatment created a fine dispersion of martensite plate cracks across the bulk, in orientations determined by the martensite habit-planes, the SC treatment led to radial, non-surface-breaking martensite plate and grain boundary cracks of different lengths and widths. Besides the cracks, these two pre-cracked samples have large grained high carbon tempered martensitic microstructures with an absence of primary carbides due to the high austenitisation temperatures and long times [26, 27]. The control sample heat treated using the standard procedure has finer lower carbon tempered martensite and primary carbides up to 1 µm in diameter.

Despite the different heat treatments and resulting microstructures, the macrohardness values of all three samples are relatively close and above the engineering requirement of 58 HRC (650 HV) [28], which allows a valid comparison of the RCF response of the samples.

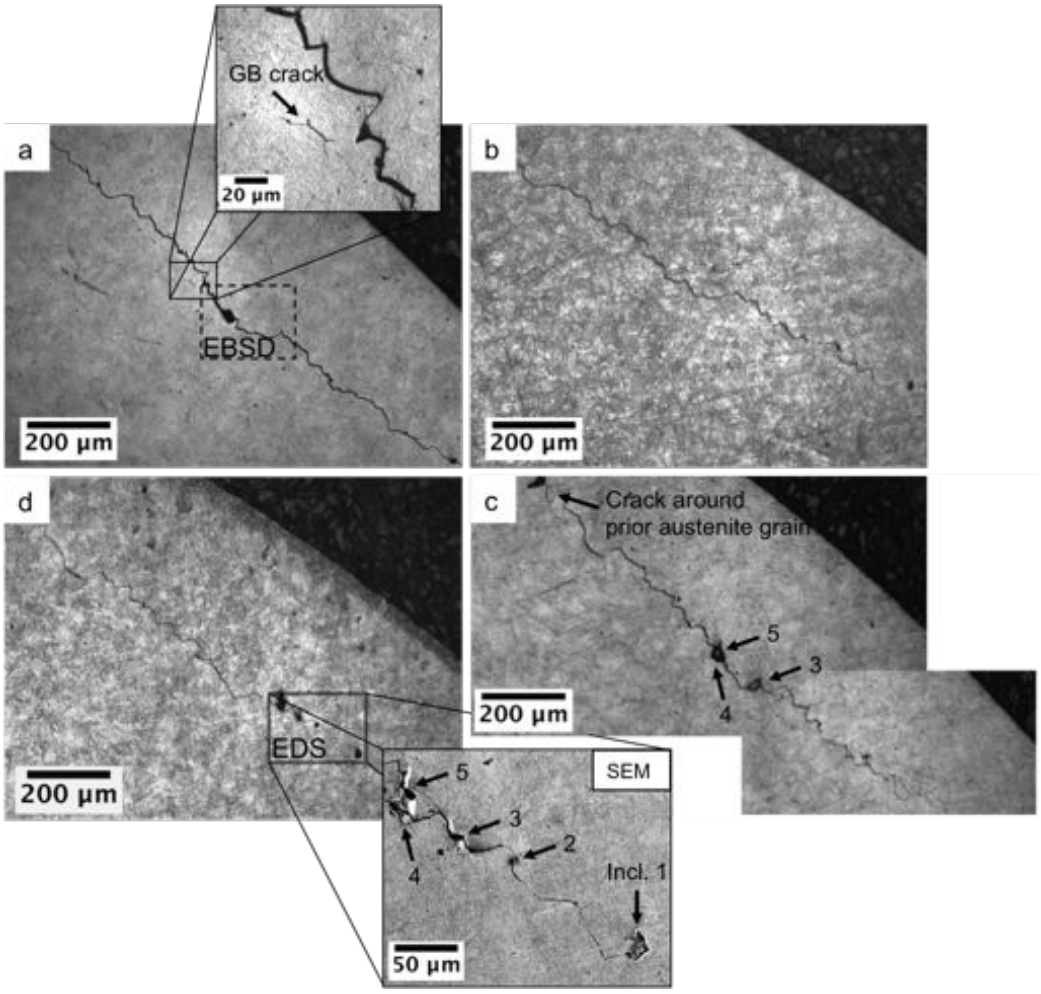

Figure 11: Large crack found in the circumferential cross section of the MPC sample showing four sectional images of the same region. In (a) is shown a smaller grain boundary crack denoting the lack of toughness, or cracking proneness, of the alloy and in (d) a series of inclusions that are likely to have been the crack initiators. The distance from inclusion 5 to the crack tip to the left is 948 µm and to the right crack tip, 738 µm.

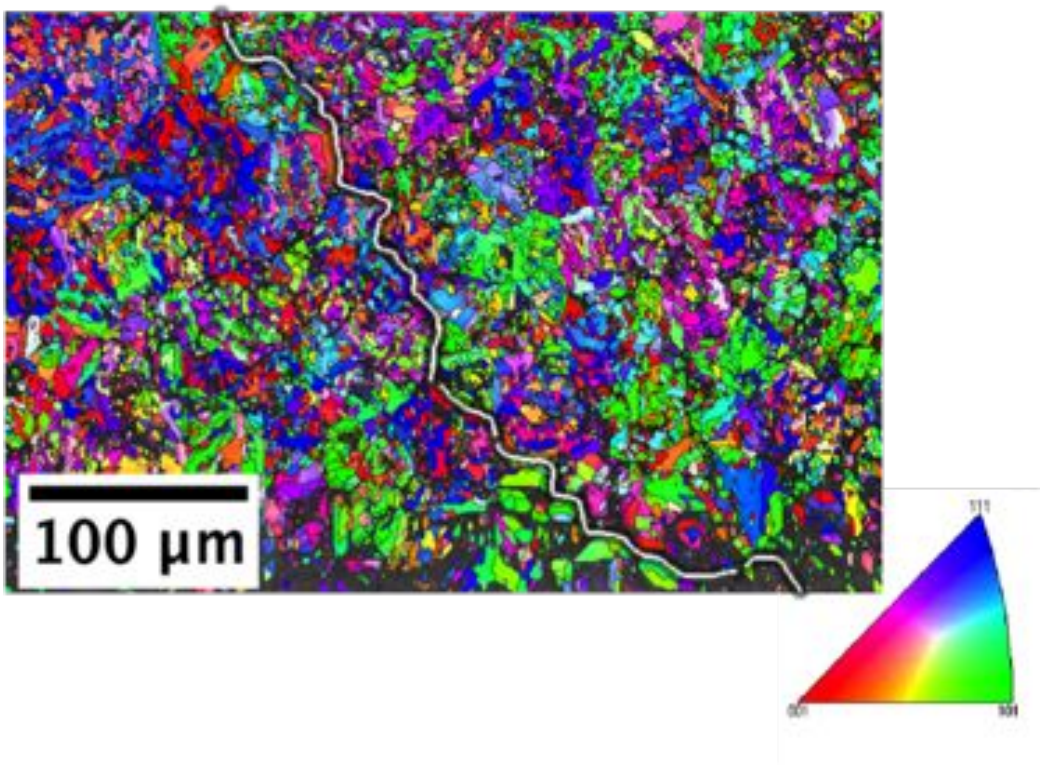

Figure 12: EBSD map (53% indexed and extrapolated to 76% using post-acquisition software) of a section of the fatigue crack (highlighted in white) in MPC sample.

Table 8: Average values of energy dispersive spectroscopy data from the matrix and WEM around cracks and inclusions (butterflies) using FIB/TEM samples and SEM samples. The inclusions that most likely originated the RCF crack of Fig. 11 and 12 were also analysed.

Sample	Region	Elemental composition (wt%)										
		Al	Si	P	S	Ca	Cr	Cu	Mn	Mo	O	Fe
L1 [SC]	WEM of butterfly	-	-	-	0.59±0.15	-	3.24±0.37	-	0.33±0.21	-	-	95.81±1.87
	Matrix	-	0.11±0.07	-	0.72±0.12	-	1.93±0.21	-	1.25±0.19	-	-	95.97±1.39
	Butterfly main inclusion	0.2±0.01	-	-	29.83±0.22	-	1.23±0.05	-	57.02±0.33	-	2.52±0.11	9.17±0.14
	Butterfly secondary inclusion	59.1±0.39	-	-	0.21±0.02	-	0.03±0.01	-	0.21±0.01	-	40.12±0.52	0.28±0.02
MPC	WEM of crack	-	0.35±0.03	-	-	-	1.65±0.15	-	-	-	-	98.00±1.95
	Matrix	-	0.45±0.03	-	-	-	1.50±0.13	-	-	-	-	98.05±1.95
EBSD1 [MPC]	Inclusion1	-	0.46±0.03	0.23±0.02	0.39±0.03	0.19±0.02	1.59±0.15	-	0.26±0.02	-	13.08±0.44	83.78±1.19
	Inclusion2	2.55±0.21	0.29±0.03	-	4.08±0.2	-	2.25±0.21	-	11.65±0.37	-	11.66±0.37	67.52±0.73
	Inclusion3	-	0.40±0.03	-	0.20±0.02	-	1.68±0.17	-	-	-	4.70±0.23	93.01±1.58
	Inclusion4	-	0.42±0.03	0.22±0.02	0.29±0.03	-	1.83±0.21	0.42±0.03	0.33±0.03	-	8.10±0.32	88.39±1.22
	Inclusion5	-	0.34±0.03	0.22±0.02	0.20±0.02	-	1.72±0.17	-	-	-	5.24±0.26	92.28±1.54

4.2. Retained austenite

The retained austenite data presented in Table 4 show a consistent trend, that V_γ increases with austenitisation temperature and time, with a tendency for decrease upon tempering and rolling contact fatigue testing.

According to Voskamp, the values of retained austenite during RCF decrease depending on the number of cycles and Hertzian pressure applied [5]. For example, for 3.5 GPa it should be 0.03 after 2.8×10^8 cycles and virtually no retained austenite after 8.6×10^8 cycles. Due to experimental limitations, the present study did not allow precise measurement of the quantity of retained austenite after RCF in the small subsurface volume that experiences the largest shear stresses, the results reflecting an averaged determination from regions subjected to different levels of stress, which explains why these values are larger than reported ones and very similar to that of the Q-T samples. To avoid this averaging, Voskamp performed repeated XRD measurements using Mo K_α radiation and a spot size of only 1 mm^2 on continuously rotating inner bearing rings with one measurement per depth level after layer removal through electropolishing of the whole ring, but such technique was not accessible in this study [5].

The larger retained austenite contents of samples SC and MPC will be shown in subsequent discussion to play an important role in the generation of WEM.

4.3. Surface roughness and RCF testing

Before analysing the RCF response of each sample in terms of WEM generation it is important to note the relationship between the cycles that each sample ran for and parameters that can lead to failure attributable to surface roughness or the consequences of retained austenite. As seen in Table 5, the surface roughness of the pre-cracked samples was lower than the crack-free one, however both control and MPC specimens ran for almost the same amount of time ($\sim$550 h). Instead, despite MPC and SC having almost identical surface roughness values and retained austenite contents, SC ran for over three times longer than MPC, indicating counterintuitively, that the subsurface case of cracks created by indenting played a key role in *enhancing* RCF life.

Microscopy demonstrated that the initial radial microscopic and grain boundary cracks in sample SC had propagated and branched, thus toughening the steel in a manner similar to the behaviour of other brittle materials [29, 30]. The indentation cracks introduced prior to RCF testing, and any cracks in martensite plates, serve to deflect the contact-stress induced fractures. The initial microscopic cracks in martensite plates are themselves randomly oriented on a macroscopic scale and hence serve the same purpose; this is evident in Fig. 8b where two roughly normal families of martensite plates, 2 and 3, had their cracks propagated and intersected in 1 causing deflection of at least five crack paths (three vertical and two roughly horizontal).

Many voids and cavities where discovered when a TEM lamella (L-2) was carved out of region 1 where the cracks intersect (Figs 10 and 8b). Evans observed similar voids in the non-WEM side and at the tips of butterfly cracks, which led him to conclude that these coalesce to form butterfly cracks at defects, and that the formation of WEM is cooperative with the propagation of such crack [31]. In the SC sample, microcracks were already present before RCF and the diffraction patters of fig. 8b reveal in b_1 (away from crack edge) an amorphous-type structure of carbides in a BCC ferritic matrix and in b_2 (closer to crack edge) the same carbide structure and a faint presence of small ferrite crystallites, i.e. WEM in its very early stages. This evidence suggests that voids do get generated during RCF but only propagate pre-existing cracks rather than creating them and that WEM generation is not cooperative [31] or simultaneous [12], but posterior to damage.

When examining the amount of WEM generated in the three samples tested, it was seen that most WEM in the MPC sample (551.2 h) occurred at depths consistent with the $\tau_{xz,max}$ (99 µm), whereas for the SC sample (1672.5 h) more counts were found in the depth of the τ_{max} (190 µm). Note that in the SC sample, the maximum depth at which cracks remain after grinding and before testing is $\sim$ 300 µm. In the case of the control sample (558.1 h), all WEM counts were related to butterfly wings and found between 10 and 100 µm deep. This is because the SC and MPC samples contain pre-existing cracks, some of which are appropriately located to begin the process that leads to WEM formation, whereas an initiation stage is necessary in the case of the control sample, and this initiation must occur in the most highly stressed region. Although it is clear from the images of fig. 5 that more WEM

regions were found in the pre-cracked samples, all three samples had similar amounts of butterfly wing WEM since all were manufactured with the same material and roughly contain the same amount of inclusions. It is also worth clarifying that the butterfly cracks of the inclusions in the control sample shown in fig. 5 are oriented either parallel or up to 45 ° to the rolling surface and that not all (fig. 5u, v, and w) exhibit WEM as butterfly cracking at inclusions occurs at different times of the RCF life, mainly depending on the inclusion depth, size, and interface with the matrix [32].

4.4. WEM characterisation

When analysing the WEM formed in RCF tested samples, it was clear that the morphology of the cracks along with the presence of primary or secondary carbides around cracks plays an important role in WEM generation.

Although no direct relationship was found between the orientation or length of cracks and WEM, crack orientation is a parameter that must interact with the subsurface shear stresses and the rolling direction. In other words, the contact-induced stresses will promote closing of certain regions of a crack or the separation of crack faces depending on the crack-orientation. In general, the narrower regions of the crack develop more WEM due to more intense rubbing of their surfaces. It is clear how the narrower cracks in the MPC sample developed more WEM than the wider ones in the SC sample, despite the fact that the latter sample survived almost three times longer (fig. 5). Nevertheless, some surface-cracks, such as those observed in fig. 5r, q, and s, appear relatively wide, possibly due to an etching effect since these cracks are in fact surrounded by WEM and do not show evidence of branching.

The location of cracks with respect to certain microstructural features also influenced WEM generation/absence and two cases were identified: 1) cracks surrounded by the tempered martensitic matrix, and 2) cracks in contact with retained austenite. It is important to bear in mind that there were no primary carbides in samples SC and MPC because of the high austenitising temperatures used, so that the wavy lines found in white-etching areas of butterfly wings for example (see inside dotted white line of fig. 8a), are not due to be elongated carbides as is sometimes claimed [31].

In the first case, fine carbides resulting from the tempering of martensite

dissolve upon crack rubbing, allowing WEM formation. As Loy and McCallum established, WEM is carbon supersaturated nanosized ferrite [10]. Due to a high austenitisation temperature and long time, all the cementite in MPC and SC samples was fully dissolved so the only dissolvable carbides to supersaturate the ferrite upon crack rubbing are tempering carbides. This was corroborated through TEM fig. 8a and b where no crystalline tempering carbides were seen near cracks, only amorphous rings likely corresponding to extremely fine carbides in the process of dissolution. In the second case, cracks under RCF acting as stress concentrators cause the stress-induced transformation of the neighbouring retained austenite into untempered martensite, which then is free from primary and secondary carbides to be dissolved into solution and form hard white-etching matter, i.e. carbon supersaturated nanosized ferrite [10, 12]. The stress-induced martensite shows dark contrast (in SEM) in the vicinity of the cracks (see fig. 9c), which should not be confused with the dark-etching regions thought to be an over-tempering of the microstructure [33, 34]. In this second case, observations tend to suggest that either very little or no WEM at all is formed for the amount of cycles tested since carbon would have to be made available through autotempering or short-circuiting via dislocation clouds, for example. Since the pre-cracked samples had more retained austenite, the cracks that after RCF were not surrounded by WEM are likely to be either formed at late stages of the RCF process, neighbouring retained austenite regions, not in the regions of maximum subsurface shear stress, or sliced in a plane in which WEM is not visible.

4.5. Nanohardness

It is well-known that nanohardness values reported in GPa differ considerably from the macrohardness HV30 values because of the small volume of material involved in the former case [35, 36]. However, the relevant fact is that the WEM is approximately 9% harder than the matrix although the indents are just a few micrometres away from the cracks (Table 7, Fig. 6). It is possible that this represents an underestimate because of the realtively small size of the WEM regions and the necessarily close proximity of WEM to the cracks. When larger regions of WEM have been studied, most reported values are found to be 30-50% harder than the surrounding matrix [9, 12] although Navas et al. reported a hardness only 5% higher than the matrix for WEM layers formed in hard-turned AISI O1 steel [37].

4.6. FIB/TEM

By analysing the images and diffraction patterns of one inclusion and a crack in the SC sample and one crack of the MPC sample, it was possible to obtain a wide spectrum of detail on the deformation mechanisms that take place during RCF and lead to the formation of WEM. The cross section of a butterfly 50 µm deep (fig. 8a) reveals three interesting features: (i) the main inclusion, later confirmed to be MnS through EDS, has a very fine grained structure as seen in the micrograph and through its ring-like diffraction pattern indexed as MnS and M_3C carbide (a_1). This structure is surprisingly similar to that of WEM (nanosized crystallites), possibly because the attached hard Al_2O_3 particles focus the strain on the soft MnS in a similar fashion as hard inclusions beat on the softer ferrite around them during RCF promoting carbide dissolution and recrystallisation that give rise to the carbon supersaturated nanosized ferrite known as WEM. (ii) At the tip of one of the butterfly cracks, a region of very small grains (a_2) was found, which was indexed as nanosized ferrite with a faint halo of amorphous-like carbide. (iii) Regions further away from the butterfly crack where no small grains were present were indexed as a single but heavily deformed ferrite crystal with a heavy presence of amorphous-like carbide.

When comparing these observations with a deflected crack, in the same sample, and 120 µm deep (fig. 8b), the cross section revealed a crack with faces widely separated, possibly propagated through the presence of voids, that had: (i) twinned regions very close to crack surfaces, possibly stress-induced mechanical twins (fig. 8b'), (ii) regions further away from cracks (b_1) that were indexed as undeformed ferrite crystals with a strong dispersion of amorphous-like carbide, and (iii) regions very close to the crack surfaces (b_2) that had a lighter amorphous-like carbide response and a weak peak of small ferritic crystallites. In conclusion, wherever there is a presence of nanosized ferrite, the amount of amorphous-like carbide seems to diminish compared to regions where ferrite is coarser and simply deformed (further away from cracks).

The inclusion and crack analysed in the SC sample had been subjected to a larger number of RCF cycles than the crack of the MPC sample (fig. 9c). However, the MPC sample shows already after 16.8 h of RCF a more densely twinned region in the vicinity of the crack (c_2) when compared with normal regions of twinned martensite away from it (c_1). There also is amorphous-like

carbide in the ferritic matrix near the crack tip. These observations seem to suggest that after the stress induced transformation of retained austenite neighbouring the crack to untempered martensite, the process of ferrite deformation through rubbing and eventual recrystallization (nanoferrite) is progressive but for the short running time of lamella 3, only the stress-induced transformation/deformation twinning took place.

4.7. EBSD

The large crack found in a cross sectional cut of the MPC sample exactly below the centre of contact (see fig. 11) was analysed through serial sectioning and EBSD which revealed at least twelve inclusions in the crack path, five of which were analysed using EDS. No WEM was observed around the crack, there were no connections with the free surface, and the crack showed wider and narrower crack sections depending on orientation relative to the rolling surface. Sections of the crack sometimes followed prior austenite grain boundaries (fig. 11c), with adjacent nascent cracks at austenite grain junctions (fig. 11a). These observations suggest this is a subsurface fatigue crack initiated at inclusions, propagated through brittle grain boundaries and arrested near the free surface due to the compressive stresses developed during RCF. The EBSD map showed that the regions to the left and right of the crack path have different orientations confirming that the crack propagates along grain boundaries. None of the inclusions entrapped in the crack path displayed signs of WEM butterfly wings despite the fact that butterflies have been shown to form after 10^5 cycles ($\sim$11 min for the testing conditions used in this study) meaning that the lack of WEM around the inclusions and fatigue crack is likely to be because they are located over 200 µm away from the regions of maximum subsurface shear stresses [38, 39].

4.8. EDS

Measurements of the chemical composition of the WEM relative to the matrix were performed in two different scenarios (Table 8). The WEM formed around an inclusion in the SC TEM sample using an EDS-STEM detector and secondly, WEM formed around a crack in the MPC SEM sample using an EDS-SEM detector. In both cases the results agree that the WEM has a higher chromium concentration than the matrix, which matches

previous EDS analyses of white-etching areas [31]. The observation cannot be attributed to, for example, the deformation-induced dissolution of Cr-rich primary carbides that are not present in the SC and MPC samples.

EDS was also used to analyse the composition of butterfly and fatigue-crack causing inclusions. The results in Table 8 confirm that the main butterfly inclusion of fig. 8a' (L-1) is manganese sulphide and the secondary inclusions are alumina. In the case of the inclusions of fig. 11, only inclusion 2 was clearly identified as a manganese sulphide with alumina encapsulation. Inclusions 1, 3, 4, and 5 appear to have fallen during preparation, but the relatively high oxygen content picked up suggest they were a family of globular oxides, which are the second most common inclusion after sulphides in 100Cr6 steel [40].

5. Conclusions

Critical experiments using a wide range of mechanical tests and characterisation tools have permitted the following conclusions regarding the white-etching matter formation in bearings:

- Evidence has been provided to show that the presence of microscopic cracks in samples prior to RCF testing leads to the formation of hard white-etching matter in their close proximity, akin to the butterfly wings in conventional bearing tests. Therefore, hard white-etching matter is likely to be a symptom of microscopic fracture rather than the cause. During rolling contact fatigue, the crack faces rub and beat against each other, creating minute grains as a result of recovery and recrystallisation, with the possibility of the mechanical solution of fine cementite playing a role. Coarse primary cementite was absent in two of the samples studied and hence its presence is not a critical requirement for WEM formation.

  The corollary of this conclusion is that WEM can in principle be mitigated by increasing the toughness of the bearing steel, or in other words, increasing the energy required for cracks to form and propagate.

- Consistent with previous work, the WEM formed around inclusions (butterflies) and cracks is essentially nano-sized ferrite with a very fine

distribution of carbide particles that is at an advanced stage of subdivision, so much so that these particles display an amorphous-like ring-diffraction pattern. This WEM was also found to be approximately 9% harder than the tempered martensitic matrix.

- In order to form WEM around cracks through the rubbing of surfaces two parameters are highly important: the width of the crack and the amount of carbides in the matrix around the crack. On the one hand, the orientation of the crack with respect to the rolling direction and the depth of subsurface shear stress will determine which part of the crack widens under the applied pressure and which contract, rub, and generate WEM. On the other hand, if austenitised in the γ phase field, cracks neighbouring retained austenite regions that strain transform to untempered martensite under RCF seem to generate less WEM due to the lack of carbides compared to cracks found in tempered martensite. Since inclusions are better stress concentrators than cracks, no retained austenite is found around them but only tempered martensite, hence why they proved to be more effective WEM generators than cracks. Carbides act as a source of carbon to be dissolved through cyclic stress and supersaturate the nanostructured ferrite crystallites, which is what hard WEM is. Without carbides in the proximity, ferrite deforms into nanosized crystallites, but does not get enriched by carbon so no hard WEM or very little is formed.

- Since the pre-cracked samples used in this work were austenitised in the γ phase field where all spheroidised carbides were dissolved, the wavy contours found in the WEM wings of butterflies are more likely to be flow marks rather than elongated carbides as previously believed.

- Just like hard inclusions under RCF are able to deform the softer steel around them by creating nano-sized ferrite with a distribution of very fine carbides, a hard oxide like alumina encapsulating a softer inclusion like manganese sulphide (duplicate inclusions) can create a nano-sized manganese sulphide structure with a very fine carbide distribution due to the beating action of the hard alumina particle.

- FIB-TEM characterisation of RCF samples confirmed the formation of voids and cavities around cracks and butterflies, which seem to widen

and lengthen the existing cracks, but no evidence was found of those voids coalescing into newly formed cracks.

- EBSD showed that fatigue cracks propagate along the prior austenite grain boundaries confirming the lack of toughness of 52100 steel despite the standard tempering treatment and the considerable amount of retained austenite found in that specific sample that would normally stifle crack growth. This subsurface crack propagated along many inclusions, which may have been its initiators.

- Despite being counterintuitive, the surface cracked sample displayed the longest RCF life of all samples (more than three times longer) although it virtually had the same surface roughness and was tested under the same conditions. Micrographs show how these subsurface microcracks toughen the steel by deflecting damage through crack branching.

6. Acknowledgements

The authors are thankful to SKF for allowing usage of the RCF rig and helping with sample preparation. Gratitude is also expressed to other members of the Phase Transformations and Complex Properties Group, especially Ed Pickering, Dr. Steve Ooi, Dr. Yan Pei, Dr. JeeHyun Kang, James Nygaard, Chris Hulme-Smith, and Catriona Yeoh for their help with experimental techniques and interesting discussions. Funding by CONACyT, the Cambridge Overseas Trust, and the Roberto Rocca Education Programme is highly appreciated and acknowledged.

[1] M.-H. Evans: Materials Science and Technology 2012, vol. 28, pp. 3–22.

[2] S. B. Hosseini: Characterization of white layers induced by hard turning of AISI 52100 steel. residual stresses, retained austenite, and temperatures: Ph.D. thesis: Chalmers University of Technology: Gothenburg, Sweden 2013,.

[3] H. K. D. H. Bhadeshia: Progress in Materials Science 2012, vol. 57, pp. 268–435.

[4] J. M. Beswick: Practical Metallography 1975, vol. 12, pp. 200–206.

[5] A. P. Voskamp: Microstructural changes during rolling contact fatigue: Ph.D. thesis: Technical University of Delft 1996,.

[6] N. Mitamura, H. Hidaka, S. Takaki: Materials Science Forum 2007, vol. 539–543, pp. 4255–4260.

[7] H. Harada, T. Mikami, M. Shibata, D. Sokai, A. Yamamoto, H. Tsubakino: ISIJ International 2005, vol. 45, pp. 1897–1902.

[8] J. Takahashi, K. Kawakami, M. Ueda: Acta Materialia 2010, vol. 58, pp. 3602–3612.

[9] R. Österlund, O. Vingsbo, L. Vincent, P. Guiraldenq: Scandinavian Journal of Metallurgy 1982, vol. 11, pp. 23–32.

[10] B. Loy, R. McCallum: Wear 1973, vol. 24, pp. 219–228.

[11] H. Swahn, P. C. Becker, O. Vingsbo: Metallurgical & Materials Transactions A 1976, vol. 7, pp. 35–39.

[12] A. Grabulov, R. Petrov, H. W. Zandbergen: International Journal of Fatigue 2010, vol. 32, pp. 576–583.

[13] K. Hashimoto, K. Hiraoka, K. Kida, E. C. Santos: Materials Science and Technology 2012, vol. 28, pp. 39–43.

[14] B. Zhang, W. Shen, Y. Liu, X. Tang, Y. Wang: Wear1997 211, (164–168).

[15] D. M. Turley: Materials Science and Engineering 1975, vol. 19, pp. 79–86.

[16] K. Ryttberg, M. K. Wedel, P. Dahlman, L. Nyborg: Journal de Physique IV (Proceedings) 2006, vol. 134, pp. 1313–1318.

[17] S. B. Newcomb, W. M. Stobbs: Materials Science & Engineering A 1984, vol. 66, pp. 195–204.

[18] W. Lojkowski, M. Djahanbakhsh, G. Bürkle, S. Gierlotka, W. Zielinski, H. J. Fecht: Materials Science & Engineering A 2001, vol. 303, pp. 197–208.

[19] H. Schlicht: Materialwissenschaft und Werkstofftechnik 2008, vol. 39, pp. 217–226.

[20] G. J: Tribological aspects of rolling bearing failures in tribology- lubricants and lubrication: Chapter 2: SKF GmbH, Department of Material Physics/ Institute of Materials Science, University of Siegen, Germany. 2011,.

[21] W. Solano-Alvarez, H. K. D. H. Bhadeshia: Submitted to Metallurgical and Materials Transactions A 2013, .

[22] Delta Research Corp.: Livonia, Michigan, USA: Ball/Rod RCF Tester Model BR-4 Users Manual 2010,.

[23] D. Glover: A ball–rod rolling contact fatigue tester: in: J. J. C. Hoo (Ed.), Rolling Contact Fatigue Testing of Bearing Steels ASTM STP 771: ASTM International, Philadelphia, USA, 1982: pp. 107–124.

[24] K. L. Johnson: Contact Mechanics: Cambridge University Press, Cambridge, U. K., 1985.

[25] M.-H. Evans, A. D. Richardson, I. Wang, R. J. K. Wood: Wear 2013, vol. 302, pp. 1573–1582.

[26] J. M. Beswick: Metallurgical & Materials Transactions A 1984, vol. 15, pp. 299–306.

[27] C. A. Stickels: Metallurgical Transactions 1974, vol. 5, pp. 865–874.

[28] E. V. Zaretsky: Materials Science and Technology 2011, vol. 28, pp. 58–69.

[29] J. Cook, J. E. Gordon, C. C. Evans, D. M. Marsh: Proceedings of the Royal Society of London A 1964, vol. 282, pp. 508–520.

[30] W. Clegg, K. Kendall, N. Alford, J. Birchall, T. Button: Nature 1990, vol. 347, pp. 455–457.

[31] M.-H. Evans, J. C. Walker, C. Ma, L. Wang, R. J. K. Wood: Materials Science and Engineering: A 2013, vol. 570, pp. 127–134.

[32] A. Marze, L. Vincent, B. Coquillet, J. Munier, P. Guiraldenq: Memoires Etudes Scientifiques Rev. Metallurg. 1979, vol. 76, pp. 165–173.

[33] K. Sugino, K. Miyamoto, M. Nagumo, K. Aoki: Trans. Iron Steel Institute of Japan 1970, vol. 10, pp. 98–111.

[34] R. O. Ritchie: Metal Science 1977, vol. 11, pp. 368–381.

[35] N. K. Mukhopadhyay, P. Paufler: International materials reviews 2006, vol. 51 (4), pp. 209–245.

[36] M. T. Oyen, R. F. Cook: Journal of the Mechanical Behavior of Biomedical Materials 2009, vol. 2 (4), pp. 396–407.

[37] V. G. Navas, I. Ferreres, J. A. Marañón, C. Garcia-Rosales, J. G. Sevillano: Journal of Materials Processing Technology 2008, vol. 195, pp. 186–194.

[38] G. B. Johnston, T. Andersson, E. V. Amerongen, A. Voskamp: Experience of element and full–bearing testing of materials over several years: in: J. J. C. Hoo (Ed.), Rolling Contact Fatigue Testing of Bearing Steels: ASTM, Philadelphia, USA, 1982: pp. 190–205.

[39] K. Furumura, Y. Murakami, T. Abe: Motion and Control 1996, vol. 1, pp. 30–36.

[40] M.-H. Evans, L. Wang, H. Jones, R. J. K. Wood: Tribology International 2013, vol. 65, pp. 146–160.